

1 **Effects of supernova induced soft X-rays on middle and upper atmospheric** 2 **nitric oxide and stratospheric ozone**

3 ¹David E. Siskind, ²McArthur Jones Jr., ^{2,3}Jeffrey W. Reep

4 ¹Computational Physics Inc., Springfield, VA, USA

5 ²Space Science Division, Naval Research Laboratory, Washington, DC, USA

6 ³ now at Institute for Astronomy, University of Hawaii at Mānoa, Pukalani, HI, USA

7
8 Corresponding authors:

9 David Siskind (dsiskind@cpi.com)

10 McArthur Jones Jr. (mcarthur.jones16.civ@us.navy.mil)

11

12 **Abstract**

13 We provide a quantitative test of the recent suggestion (Brunton et al., 2023) that supernovae
14 could significantly disrupt ozone layers of Earth-like planets through a multi-month flux of soft
15 X-rays that produce ozone-destroying odd nitrogen (e.g. NO and NO₂). Since soft X-rays do not
16 directly penetrate down to the ozone layer, this effect would be indirect and require downward
17 transport of NO_x from the mesosphere. Mirroring previous studies of the indirect effects of
18 energetic particle precipitation (EPP-IE), we call this the X-ray Indirect Effect (Xray-IE). We
19 use the NCAR Thermosphere-Ionosphere-Mesosphere-Electrodynamics General Circulation
20 Model (TIME-GCM) to simulate the production of NO and its transport into the stratosphere.
21 We model the soft X-ray flux as if it were a multi-month long solar flare and use our previously
22 developed solar flare model to simulate the soft X-ray enhancement. Our results yield significant
23 enhancement in stratospheric odd nitrogen, most dramatically in the Southern Hemisphere. The
24 strongest global effects are seen in the upper stratosphere at pressure surfaces between 1-3 hPa
25 (about 42-48 km) consistent with previous observations of the EPP-IE. We then use a detailed
26 stratospheric photochemistry model to quantify the effects of this NO_x enhancement on ozone.
27 Widespread ozone reductions of 8-15% are indicated; however, because these are limited to the
28 upper edges of the ozone layer, the effects on the ozone column are limited to 1-2%. We thus
29 conclude that the effects of a multi-month X-ray event on biologically damaging UV radiation at
30 the surface is also likely to be small.

31 **1. Introduction**

32 As discussed by Airapetian et al., (2019) and summarized by Garcia-Sage (2023), the explosion
33 of new discoveries of exoplanets and the search for life in the universe as led to increased recent
34 interest in how space weather can influence the climate and habitability of the earth and possible
35 life-bearing exoplanets. As the above articles discuss (see also Kahler and Ling, 2023), these
36 extreme space weather events can include solar/stellar flares, coronal mass ejections, solar/stellar
37 energetic particles (SEPs) and/or cosmic rays. There is, however, a parallel line of inquiry that
38 has long considered the effects of supernovae on planetary biospheres (Gehrels., et al., 2003). As
39 we will discuss, there is significant conceptual overlap in the specific mechanisms, which is a
40 motivation for our present study.

41 Recently Brunton et al. (2023) have proposed a new mechanism by which supernovae could
42 threaten the existence of planetary biospheres. The classical mechanisms have traditionally
43 invoked ozone depletion either due to gamma ray emission which would occur promptly (within
44 100 days) with the event, or from cosmic ray fluxes which could be emitted over a period on the
45 order of 10-100 years (Gehrels, et al., 2003). Brunton et al., (2023) suggest a third mechanism
46 from enhanced X-ray emissions that might result from interactions between the supernova blast
47 wave and the local interstellar medium. They present observed light curves showing X-ray
48 emissions occurring over periods ranging from 6 months to several years after the initial
49 eruption. They suggest that these emissions might represent a heretofore unexplored mechanism
50 for planetary ozone destruction.

51 An important consideration for understanding the effect of enhanced X-rays on the ozone layer,
52 which Brunton et al (2023) discuss, is the fact that X-rays with energies less than 10-20 keV are
53 absorbed in the mesosphere, above the ozone layer. While Brunton et al., recognize that there
54 may be X-ray emission from a supernova with greater energies, much of their data is limited to
55 these softer X-rays. As a result, they suggest that the effect of X-rays would be more indirect and
56 they quote some aeronomic studies (Solomon et al., 1982; Randall et al., 2006) of how
57 perturbations to nitric oxide in the mesosphere and lower thermosphere could be transported
58 down to the middle atmosphere where they would catalytically lead to ozone loss.
59 Conventionally this coupling mechanism is due the production of nitric oxide (NO) in the auroral
60 zones near 100 km altitude by energetic electron impact on N₂ followed by descent through the
61 mesosphere into the stratosphere under the cover of polar night, which limits the dissociation of
62 the enhanced NO by UV sunlight. Randall et al., (2007) labeled this as the Energetic Particle
63 Precipitation Indirect Effect (EPP-IE). Here, motivated by Brunton et al.'s hypothesis, we
64 consider an analogous indirect effect on stratospheric odd nitrogen and ozone from continual soft
65 X-ray influx, which we dub the "X-ray IE".

66 Brunton et al. (2023) provide estimates for the total amount of X-ray energy that might threaten
67 planetary ozone layers and compared them to the integrated energy emitted by a multi-year solar
68 flare. Specifically, they argue that a so-called Carrington flare (X45, i.e., $4.5 \times 10^{-3} \text{ W m}^{-2}$), near
69 the upper limit of flare energy release by the Sun (see e.g., Cliver et al 2022), would have to
70 persist for 2.8 years to provide the requisite energy. Using this analogy, we will use an existing
71 solar flare model (Siskind et al., 2022) and consider the consequences of previously considered
72 solar flares extending for over a year. We will show how the X-ray IE can lead to a significant
73 influx of nitric oxide entering the stratosphere and quantitatively model to what extent this influx
74 could reduce ozone abundances. Ultimately, we conclude that due to the specifics of how NO is
75 transported in the middle atmosphere, while significant effects are probable, the global
76 destruction of the Earth's ozone layer is less likely.

77 The general outline of the paper is as follows. In Section 2, we introduce the solar flares that
78 form the basis of our study, look at the initial response of lower thermospheric NO and compare
79 our calculations with previously published observations of the nitric oxide response to solar flare.
80 In Section 3 we document the descent of this flare-produced NO down through the mesosphere
81 using a three-dimensional model of chemistry and transport of the middle and upper atmosphere

82 (the NCAR Thermosphere Ionosphere Mesosphere Electrodynamics General Circulation Model
83 (TIME-GCM)). To validate the X-ray IE we will put it into context of our calculated EPP-IE
84 which can be compared with the extensive literature on that topic. Finally, in Section 4, we
85 perform photochemical modeling of the sensitivity of stratospheric ozone to the various
86 enhancements in middle atmospheric nitric oxide suggested by the TIME-GCM. One limitation
87 that we will discuss is that the 30 km bottom boundary of the TIME-GCM is right at the peak of
88 the ozone layer. Thus, ~~our~~ photochemical simulations are required to be able to extrapolate down
89 to encompass the entire ozone column.

90

91 **2. Solar Flare and thermospheric NO modeling**

92 2.1. Solar Flare modeling

93 Our approach follows the suggestion of Brunton et al. (2023), namely, to model the multi-month
94 soft X-ray flux as if it were a solar flare that lasted for months rather than the 30-60 minutes
95 which is typical (cf. Rodgers et al., 2010; Table 3; also Reep et al., 2023). The advantage of this
96 approach is that it allows us to utilize existing flare spectra (Siskind et al., 2022). These spectra
97 were developed with the NRLFLARE model, a physical model of solar flare irradiance, which
98 uses a series of flaring loop simulations to reconstruct the soft X-ray light curves of both
99 GOES/XRS channels, and from those loop simulations, synthesizes full spectra from
100 approximately 0.01 to 200 nm (Reep et al 2020; Reep et al 2022). The ratio of the two
101 GOES/XRS channels is commonly used as a proxy for temperature, which the model uses to
102 derive heating rates to drive those simulations (see e.g. Garcia 1994). The loop simulations are
103 run with the open-source radiative hydrodynamics code HYDRAD (Bradshaw & Cargill 2013;
104 Reep et al 2019, <https://github.com/rice-solar-physics/HYDRAD>), which solves the Navier-
105 Stokes equations for plasma constrained to travel along a magnetic flux tube. The full model and
106 spectral synthesis are described in detail in Reep et al 2022.

107 NRLFLARE was designed to reproduce X-ray spectra from solar flares, so it is important to
108 discuss the differences and similarities to supernova X-ray spectra. In both cases, the spectra in
109 soft X-rays (around 1 to 20 keV or so) are dominated by optically thin thermal bremsstrahlung
110 emission with a power law shape, with notable line emissions from hot ions such as Fe XXV (a
111 prominent line at 6.7 keV appears in spectra of both). There are two important differences.
112 First, the elemental abundances are not the same, which will cause the relative strength of the
113 emission (particularly line emission) to differ. Second, solar flares are expected to be in
114 collisional equilibrium, while supernova remnants have low enough densities that the collisional
115 timescale is long, so they are typically not in equilibrium. See the reviews by Vink (2012) for X-
116 ray emissions in supernovae and Fletcher et al. (2011) for solar flares (Sections 6 of both
117 reviews). For the purposes of calculating NO production, the exact spectral shape is less
118 important than the total soft X-ray energy input driving the atmospheric response. A key
119 assumption is that we are essentially ignoring wavelengths less than 0.05 nm. As discussed by
120 Brunton et al. (2023) these wavelengths would be absorbed much more directly into the
121 stratospheric ozone layer. Older studies (cf. Ejzak et al., 2007) did include these wavelengths and

122 this inclusion, as noted by Brunton “complicates any direct extrapolation” of those results when
 123 considering a purely soft X-ray event, as we do here. Our work is the first to use a model of the
 124 stratosphere, mesosphere and thermosphere to explicitly consider how the indirect effects of
 125 enhanced soft X-rays could affect global ozone.

126 One of the main subjects of the Siskind et al., (2022) paper was the September 10, 2017 X8.3
 127 flare and a spectrum at flare peak was presented in that paper. We will use that as our primary
 128 case. Table 1 summarizes key aspects of that flare that are relevant for this paper. First, it is
 129 important to note that in 2020, NOAA removed a 0.7 recalibration that had historically been
 130 applied to GOES 13-15 data (cf.

131 https://ngdc.noaa.gov/stp/satellite/goes/doc/GOES_XRS_readme.pdf; also Reep et al., 2022)

132 Thus, the true X-ray irradiance for older flares is 1/0.7 brighter. This means that the 2017 flare,
 133 originally labeled as 8.3 in Siskind et al. 2022 and earlier works (Qian et al., 2019; Redman et
 134 al., 2018) should be re-classified as X11.8. Table 1 shows the calculated peak energy by the
 135 NRLFLARE model as being about 12% greater than observed by GOES, thus effectively making
 136 this flare an X13.3 event. We will thus use the label “X13” to describe this event as we discuss
 137 our atmospheric simulations.

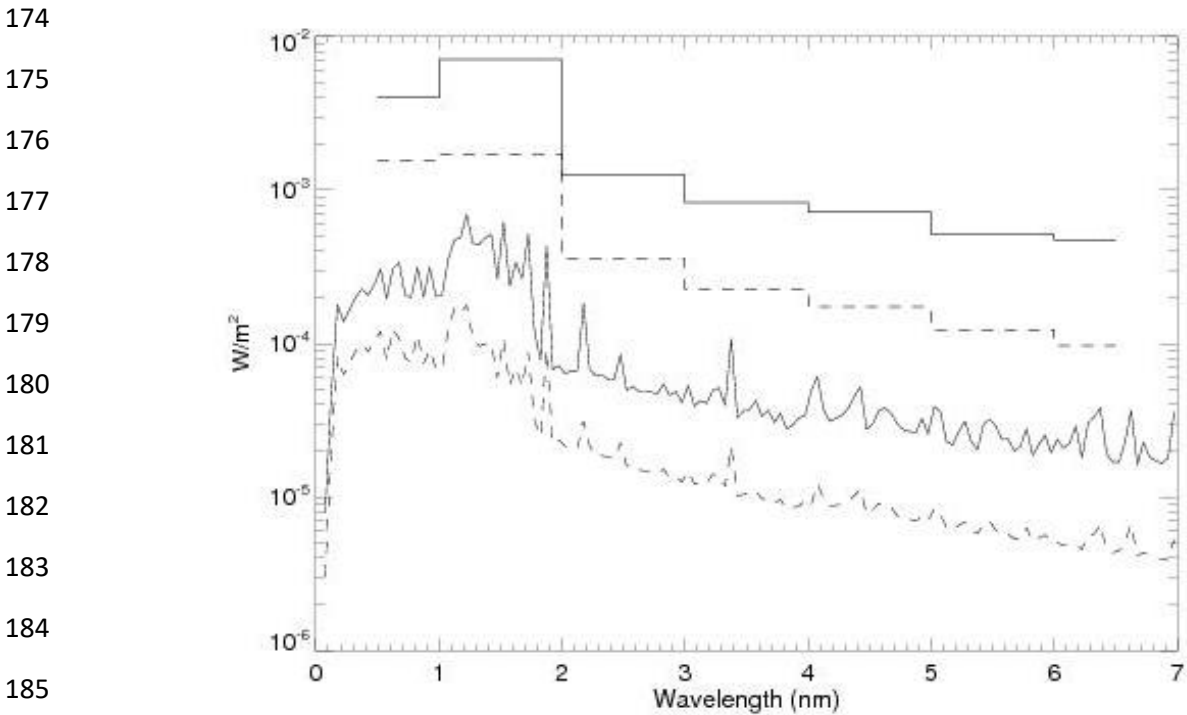
138 **Table 1**

Event	NOAA class	Calculated 0.1-0.8 X- class with NRLFLARE	Calculated energy flux, 0.1-1.0 nm (W/m ²)	Calculated energy flux, 1-2 nm (W/m ²)	Integrated energy ≥ 1 keV after 1 year (kJ/m ²)
Sept 10, 2017	11.8	13.3	1.55e-3	.0017	64.4
Oct 28, 2003	X25	X27	.004	.007	171.4

139
 140 Table 1 also shows the integrated energy in several energy bins. The division into 0.1-1.0 nm and
 141 1-2 nm bins is to compare with the calculations of Rodgers et al., (2010), discussed below. The
 142 final column extrapolates our flare duration to a year. In particular, it shows that if we assumed
 143 the X13 flare persisted for an entire year, it would deliver 64.4 kJ/m² to the atmosphere. This is
 144 less than the 400 kJ/m² that Brunton et al., (2023) use as a critical threshold for ecologically
 145 destructive X-ray energy input. We will therefore also consider the energy input from a spectrum
 146 calculated for the October 28, 2003, the so-called Halloween event. The effects of this flare on
 147 thermospheric nitric oxide were first discussed by Rodgers et al., 2010 and we will compare our
 148 calculations to theirs. Again, due to the NOAA recalibration, this flare, which was originally
 149 classified as X18, should really be classified as X25. As seen in Table 1, our calculated energy at
 150 flare peak was about 8% higher than measured by GOES and thus we label this as an X27. If this
 151 flare were to persist at peak level for a year, Table 1 indicates it would deliver about 171 kJ/m² to
 152 the atmosphere. As shown by Brunton et al. (2023, their Figure 3), it is not uncommon for
 153 supernova X-ray events to persist for over a year. Table 1 shows that if our calculated X27 event
 154 were to last about 2.3 years it would deliver about 400 kJ/m² which is the energy input postulated

155 by Brunton et al. (2023) as being biospherically destructive. Unfortunately, the problem with the
156 X27 simulation is that when this spectrum was input continuously into the atmospheric model
157 (TIME-GCM, discussed below), the model crashed after 8 days of the simulation. Thus, in our
158 discussion of ozone chemistry effects, we will discuss extrapolations based upon comparisons of
159 the nitric oxide response from the first 8 days of each simulation.

160 Figure 1 compares the spectra from our X13 and X27 calculations at their respective peak
161 minutes. The figure shows the calculated spectrum at the native spectral resolution of
162 NRLFLARE (0.5 \AA) and then integrated in 1 nm bins so that it can be compared to that derived
163 by Rodgers et al (2010, see their Figure 3). Like Rodgers et al. (2010), NRLFLARE shows a
164 significant increase in the flare spectrum from 1-2 nm relative to the shorter wavelengths less
165 than 1 nm. As discussed by Siskind et al., (2022) this seems consistent with Orbiting Solar
166 Observatory (OSO) data presented by Neupert et al., (1967), although this spectral region is not
167 well covered with modern spectra. Comparing our results in detail with Rodgers et al. (2010),
168 suggests that our calculated $0.1 - 1 \text{ nm}$ flux of $.004 \text{ W/m}^2$ is in good agreement. Our 1-2 nm
169 integrated energy is about 20% lower than Rodgers et al (2010) at flare peak. For the purposes of
170 this paper, this difference is not significant; when we compare our calculated nitric oxide
171 variation to Rodgers et al., (2010), we can account for this difference by using integrated energy
172 as the independent variable to normalize both our calculations. This will be discussed further in
173 Section 4.



187 **Figure 1.** Calculated spectra for the peak of the X27 event of October 28, 2003 (solid lines) and the X13
188 event of Sept 10 2017. The rationale for the classifications is discussed in the text. The bottom two curves

189 are at 0.5 Å resolution. The histogram format for the top two curves is the integrated energy over 1 nm
190 bins.

191

192 2.2. Atmospheric modeling with the TIME-GCM

193 The solar spectra shown in Figure 1 were used as inputs into the photoelectron ionization model
194 presented by Siskind et al., (2022) and incorporated into the NCAR TIME-GCM. The NCAR
195 TIME-GCM is a hydrostatic general circulation of the middle and upper atmosphere that solves
196 the continuity, electrodynamic, energy, and momentum equations from first principles on a
197 regular longitude and latitude and log pressure grid in the vertical (Roble and Ridley, 1994). The
198 model resolution is $2.5^\circ \times 2.5^\circ$ (longitude \times latitude) and 4 grid points per vertical scale height
199 extending from 12 to 4.6×10^{-6} hPa (or roughly 30 to 450-600 km depending on solar activity).

200 The photoelectron ionization model presented by Siskind et al., (2022) defines 12 new
201 wavelength bins for the soft X-ray energy range to give better spectral resolution (and hence
202 better altitude resolution of energy deposition) than the original NCAR spectral model presented
203 by Solomon and Qian (2005). Note, there is a typographical error in Table 3 of Siskind et al.,
204 (2022), bin #7 for the O₂ cross section. It should read 1.5E-20, not 1.5E-21. It is correctly
205 implemented in the model.

206 One difference in how we used the TIME-GCM from the short term (< 1 day) simulations of
207 Siskind et al., (2022) concerns the dynamics of the mesosphere. In the standard version of the
208 TIME-GCM (i.e., the model setup used in Siskind et al., (2022)) climatological background
209 horizontal winds, temperatures, and geopotential are used at the model lower boundary in
210 combination with monthly mean diurnal and semidiurnal tides from the Global Scale Wave
211 Model (GSWM; Zhang et al., 2010a,b). However, this standard model configuration does not
212 properly simulate the downward transport of NO_x from the mesosphere into the stratosphere. In
213 order to do so, we constrained TIME-GCM upper stratospheric and mesospheric horizontal
214 winds and temperatures between the model lower boundary (~30 km) and ~75 km with Modern
215 Era Retrospective-analysis for Research and Applications - version 2 (MERRA-2, Gelaro et al.,
216 2017) using four-dimensional tendency nudging (originally termed 4D data assimilation by
217 Stauffer and Seaman, (1990, 1994)). This nudging procedure is described in great detail by Jones
218 et al. (2018), and involves adding an additional acceleration and energy tendency term to the
219 conservation equations that is proportional to the modeled and MERRA-2 horizontal wind and
220 temperature differences up to ~75 km.

221

222 In previous studies (e.g., Jones et al., 2020; 2023), TIME-GCM was constrained using a high-
223 altitude version of the Navy Global Environmental Model (NAVEM-HA, Eckermann et al.,
224 2018; McCormack et al., 2017), which provides dynamical fields up to ~97 km. Note the
225 MERRA-2 reanalysis product used herein does not extend as high as NAVEM-HA, and
226 therefore, we had to make a small modification to equation 5 of Jones et al. (2018). This equation
227 describes the vertical weighting distribution of nudging, which in part controls the strength of the
228 additional tendency term. The vertical weighting distribution used here takes the same functional
229 form as equation (5) of Jones et al. (2018), but the z_{max} variable (representative of the TIME-
230 GCM log-pressure level where the model becomes unconstrained) is equal to -10.5 or ~75 km.

231 For reference, a vertical weighting factor of 0.5 occurs roughly at 55 km (or 0.2 hPa), above
232 (below) which the nudging term is more weighted toward TIME-GCM (MERRA-2) dynamical
233 fields. Finally, we conclude this section by noting that a key assumption that underlies our
234 approach is that all the enhanced NO_x that comes flooding into the middle atmosphere would not
235 modify ozone so dramatically as to change the circulation away from that provided by MERRA-
236 2. Based upon the (small) degree of column ozone change shown below, we conclude this is an
237 acceptable assumption, but clearly could be investigated further with a more self-consistent
238 physical model.
239

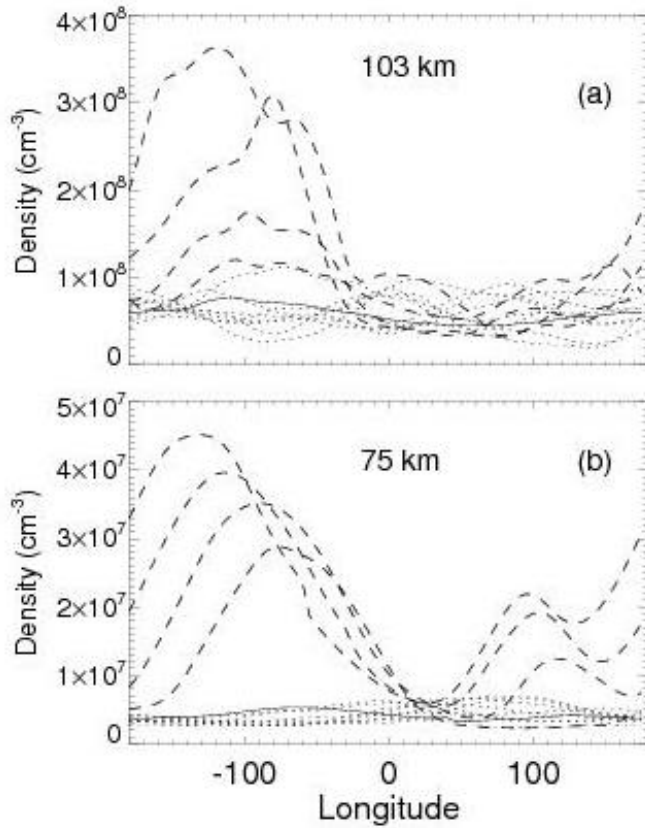
240 2.3 Initial thermospheric response to multi-month solar flare

241 As discussed above, we model the effects of supernova induced soft X-ray event as if it were a
242 multi-month solar flare. Specifically, for the X13 event, we performed a simulation which
243 continues through the end of 2017 and then covers a complete additional year. In the analyses
244 discussed below, we present the results of the X13 and X27 simulations with a baseline run that
245 only includes the EPP-IE effect. The difference between the X13 or X27 and baseline runs serve
246 to quantify the possible response of the middle and upper atmosphere to a multi-month soft X-
247 ray event. We also note that for TIME-GCM simulations performed herein geomagnetic activity
248 was held constant with $K_p \cong 3$ in order to exclusively highlight flare impacts.

249 Figure 2 shows the initial response at low latitudes (averaged from 30S-30N), plotted every two
250 hours, as a function of longitude for the first day. The solid line is 1600 UT which was just at
251 flare onset (the peak of the Sept 10, 2017 flare was around 1606 UT). The four dashed lines are
252 for 1700, 1900, 2100 and 2300 UT and show how the NO increases both in the thermosphere
253 (panel (a)) and in the mesosphere (panel (b)) immediately after flare onset. Note how the
254 longitudinal response progresses westward for the equatorial plots, tracking the sub-solar point.
255 This is consistent with our implicit assumption that the supernova will be aligned with the
256 ecliptic plane. While perhaps not always true (the galactic plane is tilted 60° with respect to the
257 ecliptic plane (cf. https://en.wikipedia.org/wiki/Astronomical_coordinate_system), any
258 supernova will nonetheless rise and set like the sun, and the peak effects will, like with a solar
259 flare, be concentrated at the sub-stellar longitude. Thus we conclude that our approach of using
260 an extended solar flare event as a means of simulating a supernova soft X-ray event is
261 acceptable. In our conclusions, we will discuss the possibility of a high latitude supernova soft
262 X-ray event further.

263 Figure 3 shows daily averaged profiles for the first 10 days for the event, both at low and at high
264 latitudes. The effects are largest at the equator, but are still significant at 59S, and extend well
265 down into the mesosphere. Note the changes appear to level off after several days, suggesting
266 that the initial response is saturating. Indeed we find that all the thermospheric response occurs in
267 the first 10-14 days. The middle atmosphere response includes both this initial effect and then
268 later, seasonal effects as NO is transported down from the upper mesosphere/lower
269 thermosphere.

270

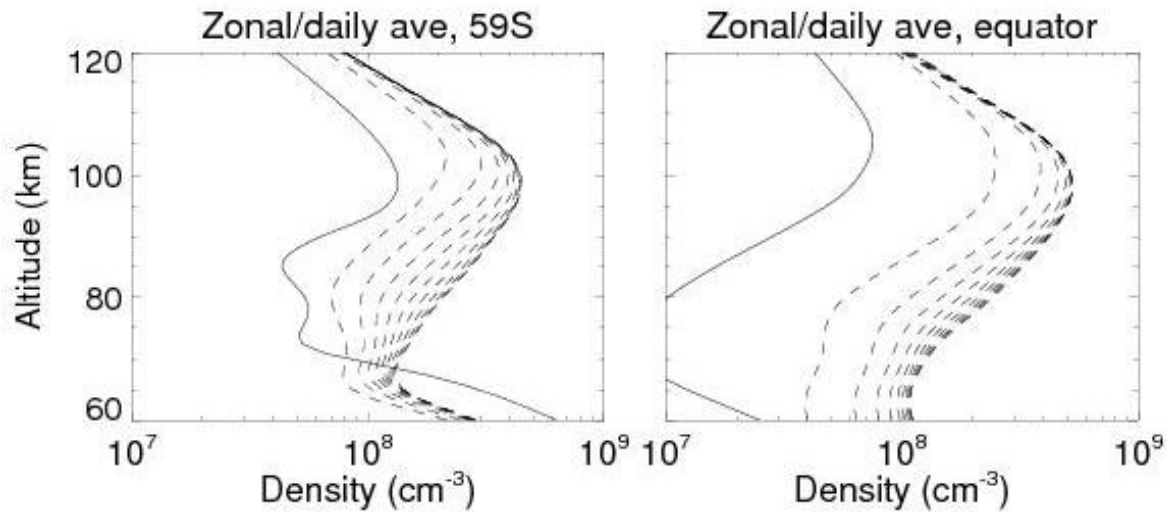


271

272 **Figure 2.** Initial response of thermospheric (panel (a)) and mesospheric (panel (b)) nitric oxide density to
 273 the onset of the extended flare. The solid line in each panel is for 1600 UT, which roughly corresponds to
 274 the onset of the flare. The dotted lines are for times prior to that. The dashed curves which progressively
 275 increase and phase to the left according to the sub-solar point are for hours 1700, 1900, 2100 and 2300
 276 UT.

277

278



279

280 **Figure 3.** Profiles of the first 10 days of the nitric oxide profile at two latitudes. The individual days are
 281 not labeled, but the day-to-day increase in NO density is monotonic with time. The solid lines are pre-
 282 flare.

283

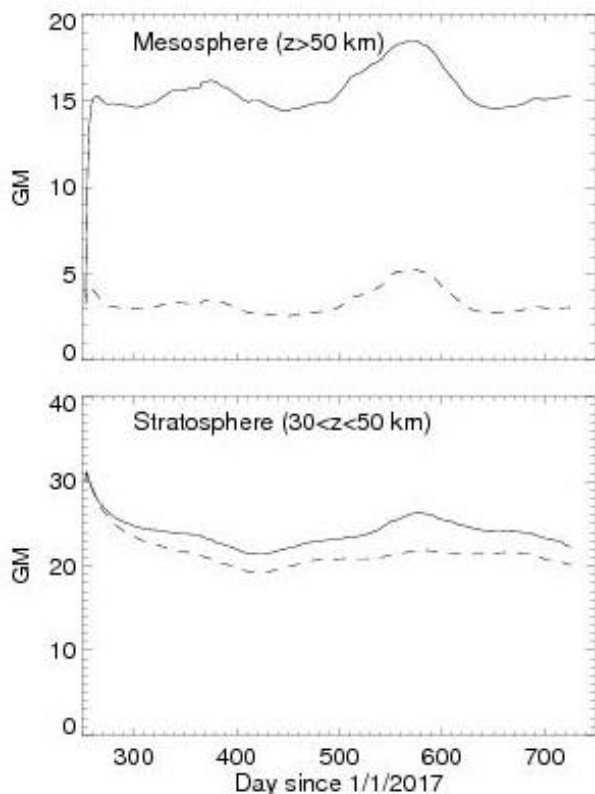
284 3. Seasonal Variation of the Xray-IE in the middle atmosphere

285 In order to provide a broad, but quantitative, overview of the production of NO_x from the
 286 extended flare/supernova, Figure 4 shows the calculated total number of NO_x molecules in units
 287 of gigamoles (GM) and compares it to a baseline/no flare simulation. This quantity has been
 288 previously used (Vitt and Jackman, 1996; Siskind et al., 2000; Funke et al., 2005) as a way of
 289 quantifying space weather impacts on the ambient NO_x budget. Here, the production of NO_x is
 290 mostly in the mesosphere while the impacts on ozone are in the stratosphere. Therefore, using
 291 the 50 km level as an arbitrary dividing line, we break out our calculation to illustrate
 292 mesospheric NO_x (top panel of Figure 4) and stratospheric NO_x (bottom panel of Figure 4)
 293 separately.

294 In each panel, the upper (solid) curve is the NO_x with the extended flare calculation. The dashed
 295 curve is a baseline case with no flare. First, considering the no flare case, our stratospheric value
 296 equilibrates to around 20-22 GM (we attribute the initial decrease to an excess of NO_x in the
 297 initial conditions). Given that the model bottom boundary is 30 km and that significant NO_x lies
 298 below 30 km, our result is likely consistent with previous estimates by Vitt and Jackman (1996)
 299 of 29-30 GM for the stratospheric production of NO_x from N₂O oxidation. For the no flare case,
 300 the upper panel shows a value between 3-5.5 GM due to the background secondary NO_x
 301 maximum in the upper mesosphere/lower thermosphere.

302 For the flare case, the mesospheric results show a rapid increase to over 15 GMs. The
 303 stratospheric NO_x does not increase immediately, but as evidenced by the increasing divergence
 304 between solid and dashed curves, shows a gradual increase in the flare produced NO_x. It is

305 interesting that for all 4 curves, the maximum NO_x occurs in the period from days 570-620. This
 306 corresponds to August and September and coincides with the late winter period in the Southern
 307 Hemisphere. As we will discuss, satellite analyses have indicated that the maximum delivery of
 308 upper mesospheric/lower thermospheric NO_x to the stratosphere occurs during that time and, as
 309 we show below, this is indeed the case here.



310
 311 **Figure 4. Total globally integrated NO_x (=NO + NO₂) number of molecules (GM: gigamoles) for**
 312 **the baseline no flare case (dashed line) and the continuous soft X-ray flare (solid line) for the**
 313 **mesosphere (top panel) and stratosphere (bottom). The soft X-ray event, which assumes a spectrum**
 314 **from the Sept 10, 2017 flare, is assumed to have begun on that day (day 253 of 2017).**

315
 316 Finally, we can give a crude comparison of the global effects of this extended flare to previous
 317 space weather phenomena. The largest difference in the stratosphere between the flare and
 318 baseline, as shown in the bottom panel of Figure 4, is ~4.5 GM. This can be compared to the 1.3
 319 GM that Funke et al., (2005) estimated was delivered to the upper stratosphere during the 2003
 320 Antarctic winter which followed a period of elevated space weather activity. Thus the extended
 321 flare appears to exceed that by about a factor of 3.5. Funke et al., (2005) also estimated a
 322 roughly equivalent amount of NO_x would end up in the lower stratospheric polar vortex, below
 323 our 30 km bottom boundary. Siskind et al., (2000) also estimated a peak vortex amount of about
 324 0.8-1.3 GM. If we assume this rough equivalence between upper stratospheric and lower
 325 stratospheric polar vortex delivery applies here, then we arrive at an estimate of 9 GM from this

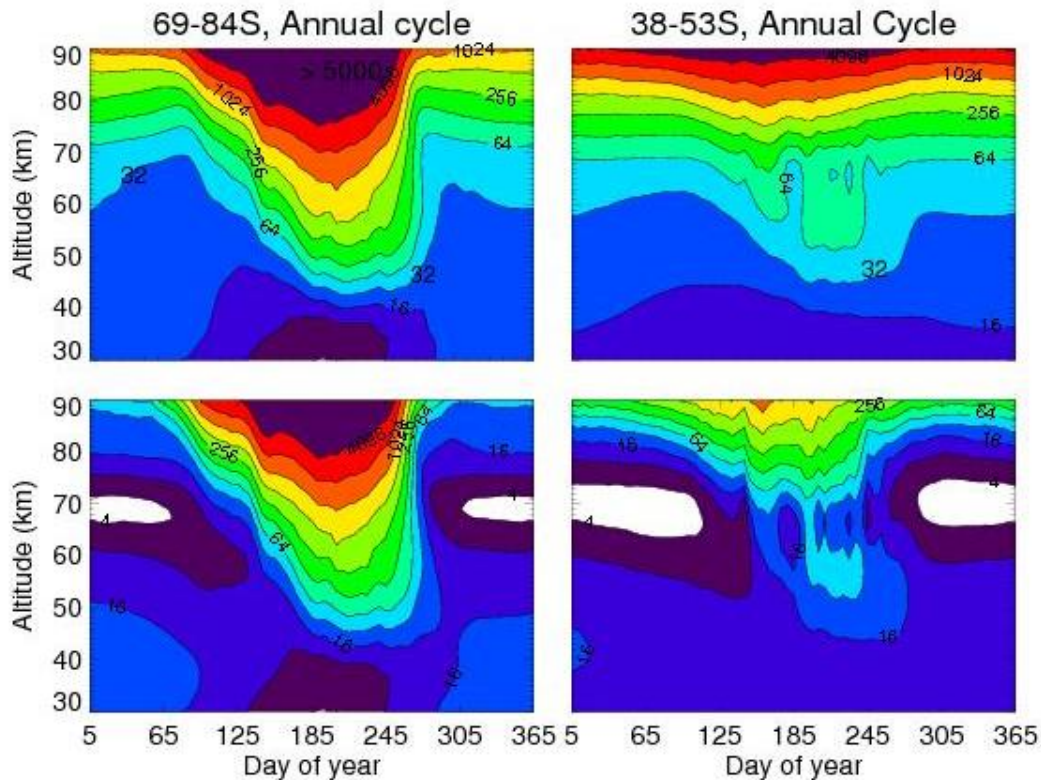
326 extended X13 flare. By comparison, Vitt and Jackman (1986) estimated a total production of 7
327 GM from the large solar proton event in 1989. Thus our current simulation exceeds any
328 previously documented space weather effect on stratospheric NO_x, but at the same time, it is not
329 dramatically bigger. As we shall see when we look at the details of the NO_x distribution and its
330 effects on ozone, our results follow that pattern i.e., greater, but not dramatically so.

331 Figure 5 compares the seasonal variation of the TIME-GCM NO_x (defined as NO + NO₂) from
332 our extended flare calculation with our baseline run that only includes the EPP-IE. It thus shows
333 the seasonal variation of how the Xray-IE leads to NO_x buildup in the middle atmosphere
334 beyond that caused by energetic electron precipitation. To understand this, we first focus on our
335 baseline EPP-IE simulation and how it compares with the recent simulations of the EPP-IE from
336 Pettit et al., (2021), specifically their Figures 9-10 which they compared with Michelson
337 Interferometer for Passive Sounding (MIPAS) data in the Southern Hemisphere. Ultimately, we
338 will conclude that the Xray-IE shows similar behavior to the EPP-IE simulation, except with a
339 larger magnitude and for a more prolonged seasonal duration. Thus to highlight the longer
340 impact, we show the entire year whereas Pettit et al., (2021) just showed April-October.

341 In comparing with Pettit's results, we see that our baseline simulation underestimates the descent
342 of the MIPAS NO_x data at the higher latitudes. The MIPAS data show the 16 ppbv contour
343 descending to below 35 km for the month of August, whereas our simulation (panel a) has this
344 contour remaining above 40 km for the late austral winter period. There are likely two reasons
345 for this. First, is likely the simple fact that TIME-GCM has a bottom boundary at 30 km and thus
346 the descent will decay as this boundary is approached. Indeed, analyses of data from both the
347 Halogen Occultation Experiment (HALOE) on board the Upper Atmospheric Research Satellite
348 (UARS) and Polar Orbiting Aerosol Measurement (POAM) data have shown that enhanced NO_x
349 can routinely be detected below 30 km in the Southern Hemisphere (Siskind et al., 2000; Randall
350 et al., 2007). Second, our model does not have the medium energy electron ionization that Pettit
351 et al., (2021) discuss. They show that models without this component of energetic electrons
352 underestimate the descent of NO_x into the mid-stratosphere.

353 On the other hand, our baseline simulation does much better at mid-latitudes (38-53S in the
354 figure). It shows the 16 ppbv contour dipping down to 45 km for a couple of months. This is
355 quite similar to the MIPAS data shown by Pettit et al., (2021) and is consistent with Funke et al
356 (2005) and Arnone and Hauchecorne (2011) who pointed out that there are two components to
357 the descent of upper atmospheric NO_x into the stratosphere. One component is directly into the
358 stratospheric polar vortex and descends down into the mid-stratosphere; as we note above, our
359 model cannot capture this. However, there is a second component that is dispersed into middle
360 latitudes in the upper stratosphere. It appears that our model does capture this and it could be
361 argued that from a global biospheric perspective, this second component is more important since
362 a greater region of the globe is affected.

363



364
 365 **Figure 5.** Annual cycle of NO_x descent into the upper stratosphere from TIME-GCM for two latitude
 366 bands. The bottom row is for a baseline simulation that only includes the EPP-IE. The top row
 367 additionally includes the Xray-IE from the X13 simulation presented in Figures 1-3. The year shown is
 368 2018 thus representing the period about 4-12 months after flare onset on Sept, 10, 2017. The values on the
 369 contour labels are in units of ppbv. The white colored regions in the baseline run are for mixing ratios < 4
 370 ppbv.

371 Regarding our Xray-IE simulation, dramatic effects are clearly seen in the mesosphere, both mid
 372 and high latitudes. The mesospheric minima near 70 km are completely filled in and mixing
 373 ratios of over 32 ppbv, up to near 100 ppbv, are seen for most of the year. However, for
 374 considerations of impacts on ozone, we focus more on the stratospheric effects. Here, at first
 375 glance, for the higher latitudes, the IE-Xray effect appears somewhat muted. We see no
 376 difference in the maximum value of NO_x descending below 50 km between our baseline and
 377 constant X13 simulation. However, the IE-Xray effect is somewhat more prolonged in its NO_x
 378 enhancement. The baseline simulation shows the 16 ppbv contour curving sharply upward
 379 around Day 270. Thus NO_x values near 50 km decrease abruptly and this is similar to what is
 380 seen in Pettit et al.'s MIPAS data. However, the X13 simulation shows the upper stratospheric
 381 NO_x values remaining between 16-32 ppbv for the entire austral spring.

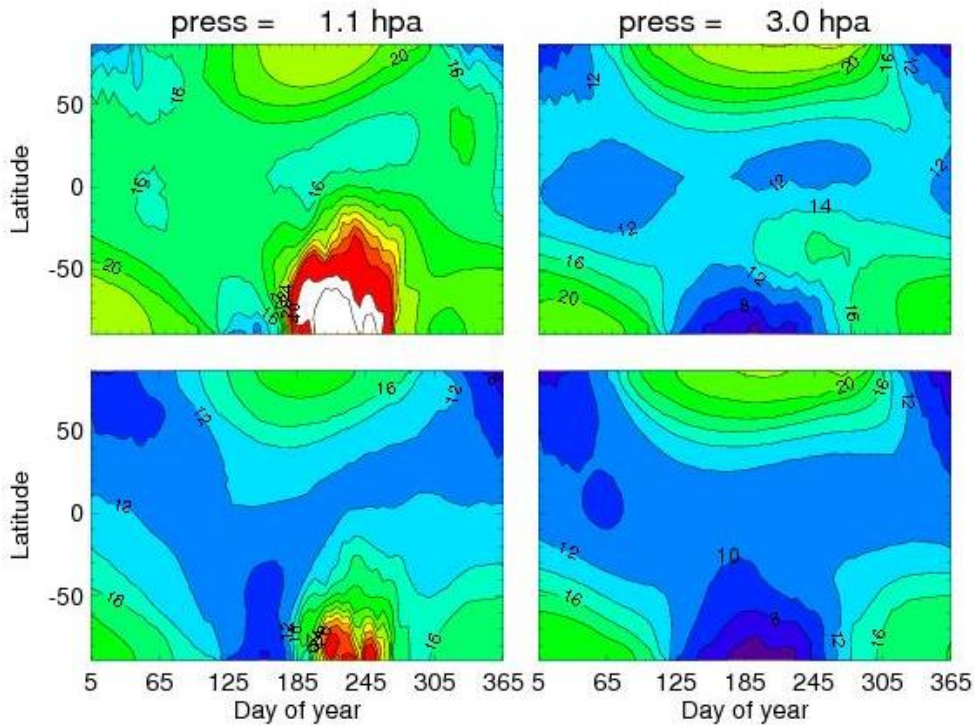
382 At mid-latitudes, the effect of the continual soft X-ray flux is more pronounced. Whereas the
 383 baseline simulation shows 16 ppbv descending to about 45 km, the flare simulation has about
 384 double that. Like the high latitude case, after approximately Day 270, the baseline case NO_x
 385 values fall below 16 ppbv, in agreement with the MIPAS data. By contrast, in the X13

386 simulation we see NO_x values of 32-64 ppbv descending to 45-50 km and the entire upper
387 stratosphere remains flooded with enhanced NO_x values greater than 16 ppbv for the whole year.

388 Figure 6 also compares our baseline (EPP-IE only) simulation with that including the Xray-IE,
389 this time for two pressure surfaces as a function of latitude and time: one near the stratopause
390 (the indicated pressure roughly corresponds to altitudes of 45-48 km) and one lower down
391 towards the middle stratosphere (approximately 38-40 km). The figure shows how the NO_x from
392 the flare/supernova spreads over the Southern Hemisphere. It is useful to first look at our
393 baseline case; it clearly shows that the EPP-IE effect is mainly in late winter/early spring in the
394 Southern Hemisphere and covers the latitudes from -80 to about -20 or -30. Note, there is no
395 evidence for this seen at 3.0 hPa whereas in actuality, there should still be a spring time
396 enhancement in the highest latitudes as we discussed above. When we compare this with the top
397 row in the figure, the effects of the soft X-rays are very apparent. The late winter/spring
398 enhancement at 1.1 hPa is about twice as large and there is now seen an enhancement at 3.0 hPa
399 whereby values of NO_x of 10-12 ppbv at Southern mid-latitudes are now replaced by values of
400 14-16 ppbv. Importantly, there is no evidence for significant enhancements in the Northern
401 Hemisphere although there does seem to be a general global increase in NO_x of about 2 ppbv-
402 about 20% above the baseline values. This lack of significant NH enhancement is consistent with
403 observations of the EPP-IE which show generally weaker effects in the NH relative to the SH
404 (Funke et al., 2014). This is generally believed to be due to the weaker descent in the NH and the
405 greater horizontal mixing due to mesospheric planetary waves (Siskind et al., 1997), although
406 NH enhancements are seen in specific years with very strong dynamical perturbations (cf. Funke
407 et al., 2017). In the present case, while we will consider the effects on stratospheric ozone below,
408 it does suggest a limit as to how biospherically destructive the soft X-ray event could be since
409 the effects are likely to be much more muted in the NH

410 One final consideration in looking at the annual cycles in the upper stratosphere mesosphere in
411 Figures 5 and 6 is that there appears to be no evidence for any continual buildup of NO_x. The
412 NO_x at the end of 2018 is not much different than at the beginning. This is consistent with
413 Figure 3 in that the day-to-day NO increase in the thermosphere decreases such that after 10 days
414 the NO profile showed little change. This will be important when we try to extrapolate from our
415 X13 simulation to stronger events.

416 Figure 7 shows the global change in ozone for the X13 simulation compared with our baseline
417 EPP-IE only case for four pressure surfaces ranging from 0.68 to 3.0 hPa. The ratios are less than
418 1.0 globally for the entire year which means lower ozone for the X13 simulation. However, there
419 is a clear maximum in the reduction for the late winter/early spring period in the SH, consistent
420 with the global distribution of the enhanced NO_x shown in Figure 5. Note that the fractional
421 reduction is larger at the lowest pressures. Normally, at these altitudes in the lower mesosphere,
422 ozone loss is dominated by the HO_x catalytic cycle (Brasseur and Solomon, 2005). However,
423 with NO_x enhancements on the order of 100 ppbv, the NO_x catalytic cycle can dominate up to
424 higher altitudes (lower pressures) than is conventional. At the same time, since the bulk of the
425 ozone density is in the stratosphere, the effect of a 3-4% reduction at 3.0 hPa is of greater impact
426 than a 10% reduction at 0.68 hPa.

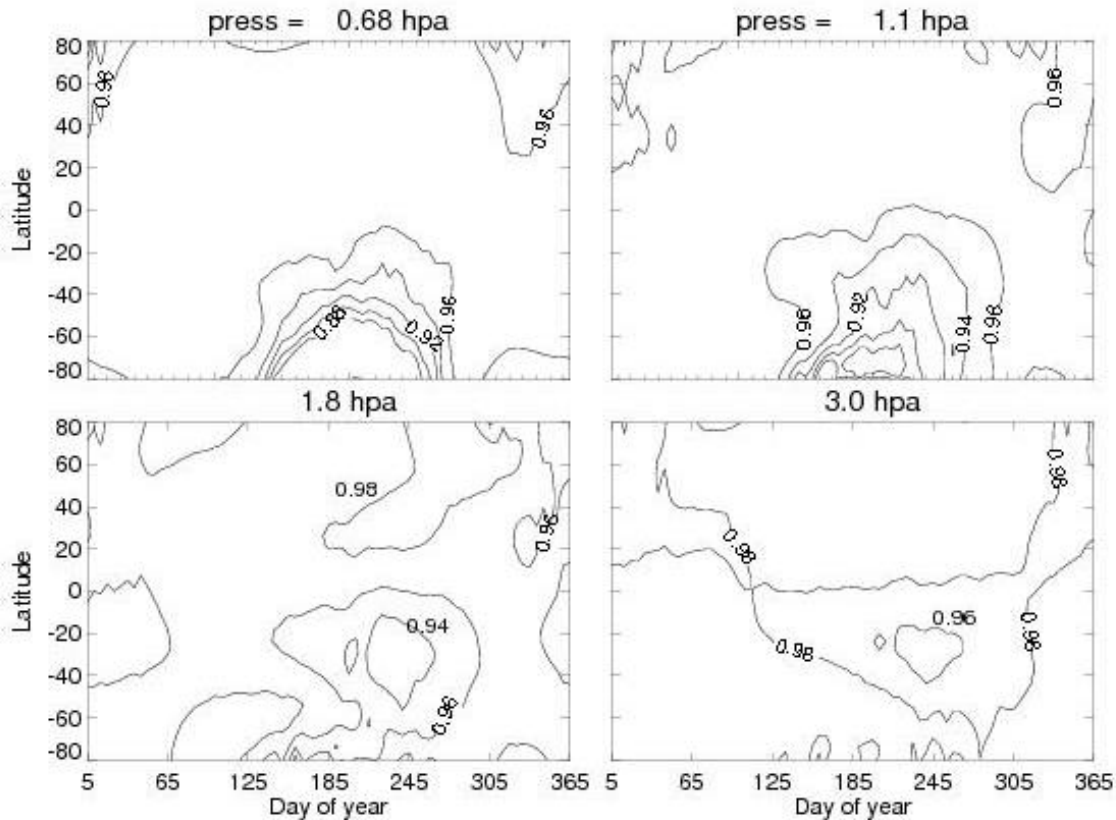


428

429 **Figure 6.** NOx (ppbv) vs latitude and day of year. The period of time is the same as shown in Figure 4.
 430 The bottom row is for the baseline case without enhanced soft X-rays; the top row includes the
 431 continuous X13 flux. The red regions are NOx values greater than 28 ppbv; the white regions are NOx
 432 values greater than 40 ppbv.

433

434 The results show here clearly suggest a potentially global effect on the ozone, albeit limited to a
 435 couple of months when the SH NOx enhancement has spread to the equator. The effect is not
 436 large- about 5% locally in the upper stratosphere and thus unlikely to be biospherically
 437 significant. However, there are important caveats to this statement that we will explore in the
 438 subsequent section. First, as we noted above, our input X-ray energy is much smaller than the
 439 supernova soft X-ray events postulated by Brunton et al., (2023). Second, the TIME-GCM is
 440 limited by a bottom boundary at 30 km. About half of the stratospheric ozone column lies below
 441 this altitude and must be considered before drawing any conclusions. We consider both these
 442 issues in the sections below.



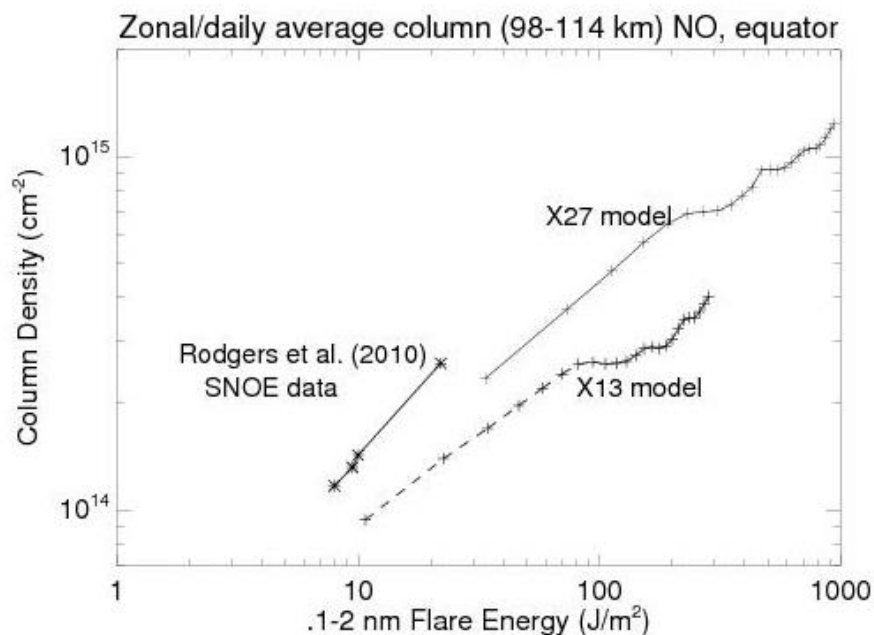
443
 444 **Figure 7.** Annual variation of the ratio of ozone from the X13 simulation compared with the baseline
 445 simulation at the four indicated pressure surfaces

446
 447 **4. Extrapolation to higher X-ray fluxes and impact on stratospheric ozone**

448 To extrapolate our NO/flare response, we first seek to compare our results with observations of
 449 the NO response to solar flares. The only quantitative data analysis of the response of nitric
 450 oxide to a solar flare that we are aware of is that by Rodgers et al. (2010) using data from the
 451 Student Nitric Oxide Explorer (SNOE). SNOE was particularly well suited to study the NO
 452 response to a solar flare because it was in a sun-synchronous orbit with an equator crossing time
 453 in the late morning when the sun was relatively high in the sky. Rodgers et al. calculated the NO
 454 column change observed by SNOE and plotted it versus the integrated soft X-ray input energy
 455 derived from a catalog of 11 flares.

456 Figure 8 compares the TIME-GCM results to Rodgers. The figure shows the integrated energy
 457 from the four strongest X-class flares observed by SNOE with the largest being the so-called
 458 Halloween event of October 28, 2003. As noted above, this event, labeled as X18 in Rodgers et
 459 al.'s Table 3, is now recalibrated to be X25, and in our simulation with NRLFLARE it is a bit
 460 higher at X27. Also shown are the TIME-GCM calculated hourly column NO from the local

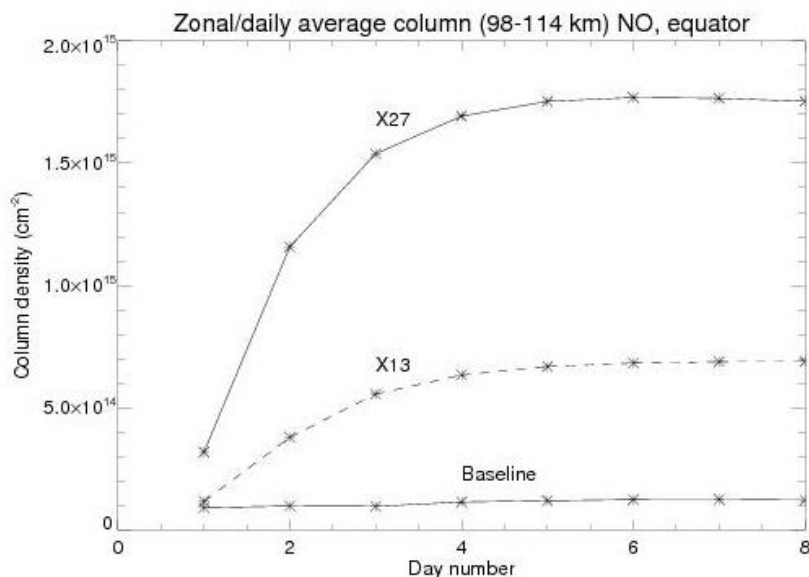
461 equatorial sub-solar longitude for each of the first 24 hours of our model simulations for the X13
462 and X27 events.



463
464 **Figure 8.** Calculated TIME-GCM NO column density enhancement from the X13 and X27 simulations
465 compared with the observed NO increases reported by Rodgers et al. (2010) for the 4 strongest flares
466 listed in their Table 3. The plus symbols on the model curves represent output for every hour. The first
467 points shown for each of the model account for the number of minutes after each integral hour that the
468 flare peaked. Thus the X13 flare peak was at 16.1 UT (cf. Table 1 of Siskind et al., 2022) and thus the
469 first point shown for the X13 model represents 54 minutes of photon flux. Like Rodgers et al. (2010), we
470 subtracted the pre-flare NO column in the model before calculating the enhancements shown.

471
472 In general, the figure shows a quasi-linear relationship between column NO and the integrated
473 energy for both SNOE and the two model simulations. It appears that the rate of energy input is
474 important for the NO increase. Thus after two model hours, the X13 simulation accrues the same
475 energy input as the 27 minute long October 28, 2003 flare and yet the NO column response is
476 well below the observations. The column NO for the X13 simulation takes over 4X the energy
477 input of the observed flare to reach the same enhancement as observed by SNOE. The column
478 NO for our X27 simulation, which is designed to simulate the October 28, 2003 flare comes
479 closer and matches the SNOE data just after the first hour of the model simulation (actually 51
480 minutes since the flare peak was at 9 minutes past 11 UT and model output was only saved
481 hourly). However, since the actual October 28 flare only lasted 27 minutes, it means that the
482 TIME-GCM is calculating a smaller NO column for the same energy input than was recorded by
483 SNOE. Rodgers et al. (2010) reported an observed column enhancement of $2.6E14 \text{ cm}^{-2}$ for solar
484 X-ray input of 22.4 J/m^2 where, reading from the graph, the TIME-GCM requires closer to 40
485 J/m^2 before reaching this level of NO enhancement.

486 After 24 hours, Figure 8 shows that the X27 simulation produces about a factor of 3 more NO
 487 than the X13 simulation. Figure 9 shows the daily averaged, zonal mean column NO for both
 488 models extended out to the full 8 days of the X27 simulation before the model crashed. Similar
 489 to Figure 3, it shows that both models level out after several days. The ratio of the two column
 490 densities equilibrates to a slightly smaller value than seen in Figure 8, about a factor of 2.6. The
 491 fact that the column densities level out can offer a useful guide for extrapolating our middle
 492 atmosphere NO_x enhancements even without completing a full year with the X27 simulation. It
 493 suggests that the reasonable enhancements might lie in the range of a factor of 2-3 over the X13
 494 simulation. In terms of GM as presented in Figure 4, it may suggest a net delivery to the
 495 stratosphere of 20-26 GM for the X27 case. We will consider the consequences of this below.

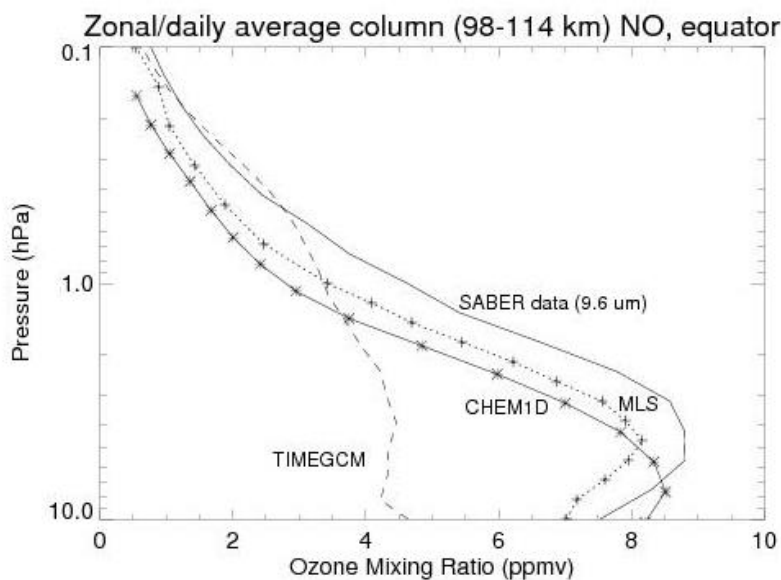


496
 497 **Figure 9.** Daily and zonally averaged equatorial column densities for the X27 (solid line with stars) and
 498 X13 (dashed line with stars) TIME-GCM simulations. A baseline case run for the conditions of
 499 September 2017, but with no flare/supernova and which remains at approximately $1 \times 10^{14} \text{ cm}^{-2}$ is also
 500 shown.

501 To evaluate in detail how ozone may be reduced for the X27 simulation, we will use the
 502 CHEM1D photochemical box model. This model has previously been used to model satellite
 503 observations of mesospheric OH (Siskind et al., 2013) and validate ground-based measurements
 504 of ClO (Nedoluha et al., 2020). It is important to first evaluate the model's ability to calculate
 505 stratospheric ozone since, as is most recently discussed by Diouf et al. (2024), chemical models
 506 of upper stratospheric and lower mesospheric ozone historically fall short of fully reproducing
 507 observations.

508 Figure 10 shows a comparison of CHEM1D and TIME-GCM ozone with two observations from
 509 September 2nd, (Day of year 245) 2018 at a latitude of 38-40S. This period and location was
 510 selected because it corresponds to the time and location of the most significant upper
 511 stratospheric ozone depletions indicated by the TIME-GCM in Figure 6. The observations are
 512 from the 9.6 μm measurement of the Sounding of the Atmosphere with Broadband Emission

513 Radiometry (SABER) instrument on board the NASA TIMED satellite and the Microwave Limb
 514 Sounder (MLS) from the NASA Aura satellite. SABER and MLS data have long been the
 515 standards for measuring middle atmospheric ozone globally. Figure 10 shows, first, that TIME-
 516 GCM is ill suited for model-data comparisons of stratospheric ozone. This is perhaps not a
 517 surprise- the model was designed to study middle atmospheric dynamics and transport and its
 518 coupling to the upper atmosphere (Roble et al., 1994). For example, TIME-GCM does not
 519 include all the active chlorine and nitrogen species that are required for a comprehensive model
 520 of stratospheric ozone. Thus for chlorine, TIME-GCM has Cl and ClO, but not HOCl. For
 521 nitrogen, TIME-GCM only has NO and NO₂, but not HNO₃ or N₂O₅. By contrast, CHEM1D
 522 does include these species. The comparison with CHEM1D very closely matches that seen by
 523 Siskind et al. (2013), who used CHEM1D for mesospheric ozone and hydroxyl and Diouf et al.
 524 (2024), who used the model of Bertaux et al. (2020) and compared with MLS ozone and SABER
 525 O₂(¹Δ) 1.27 μm emission. In all cases, the model falls short of completely reproducing the
 526 observations. Both Siskind et al. (2013) and Diouf et al. (2024), having exhausted all possibilities
 527 for reaction rate changes and possible temperature inputs, invoked the possibility of an additional
 528 source of ozone from vibrationally excited oxygen as hypothesized by Slanger et al., (1988) and
 529 Price et al., (1993). The purpose here is not to answer this long-standing question; rather, Figure
 530 10 shows that CHEM1D does as well as could be expected given our understanding of middle
 531 atmospheric ozone photochemistry. Our purpose here is to perform sensitivity studies for varying
 532 amounts of NO_x, guided by our TIME-GCM simulations. Figure 10 shows that CHEM1D is
 533 adequate for this task. We should additionally note that as one moves towards higher pressures
 534 greater than 5 hPa, the chemical lifetime of ozone becomes longer such that it is no longer under
 535 pure chemical control but also dynamical influences. Thus, the apparent improved agreement
 536 with the observations near 10 hPa should not be over-interpreted.

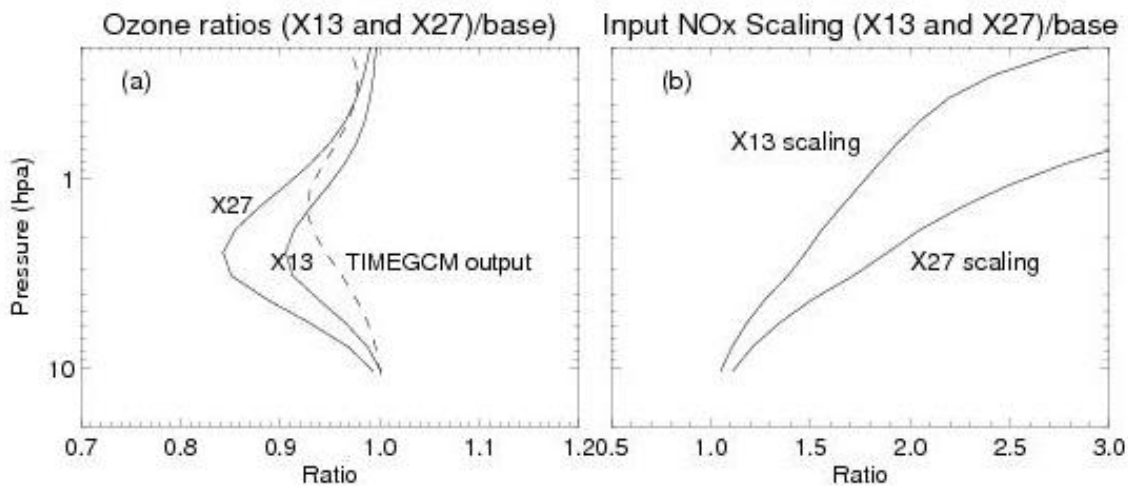


537
 538 **Figure 10.** Comparison of the TIME-GCM (long dashes) and CHEM1D (solid line with stars) models
 539 with SABER (solid line) and MLS (dotted line with plus symbols) observations of ozone. The location is

540 38-40S and the time of year is September 2nd, 2018. CHEM1D used temperature and pressure and NO_x
541 abundances from the TIME-GCM as input. The approximate altitude range corresponding to the y-axis is
542 about 30-62 km.

543 We now show the fractional ozone depletions, as a function of pressure, from the enhanced NO_x
544 due to a multi-month solar flare. Figure 11 presents the calculated ozone loss ratios (panel a) for
545 two models of CHEM1D that use enhanced NO_x compared with the baseline simulation
546 presented in Figure 10. The location and time of year is the same as in Figure 10. The NO_x
547 enhancements (panel b) are taken from the X13 simulation shown in the previous figures plus an
548 extrapolated enhancement (the greater of the curves in Figure 10) based upon the short-term
549 response shown in Figure 9. Figure 11 also shows the vertical profile of the TIME-GCM ozone
550 change taken from Figure 7.

551



552

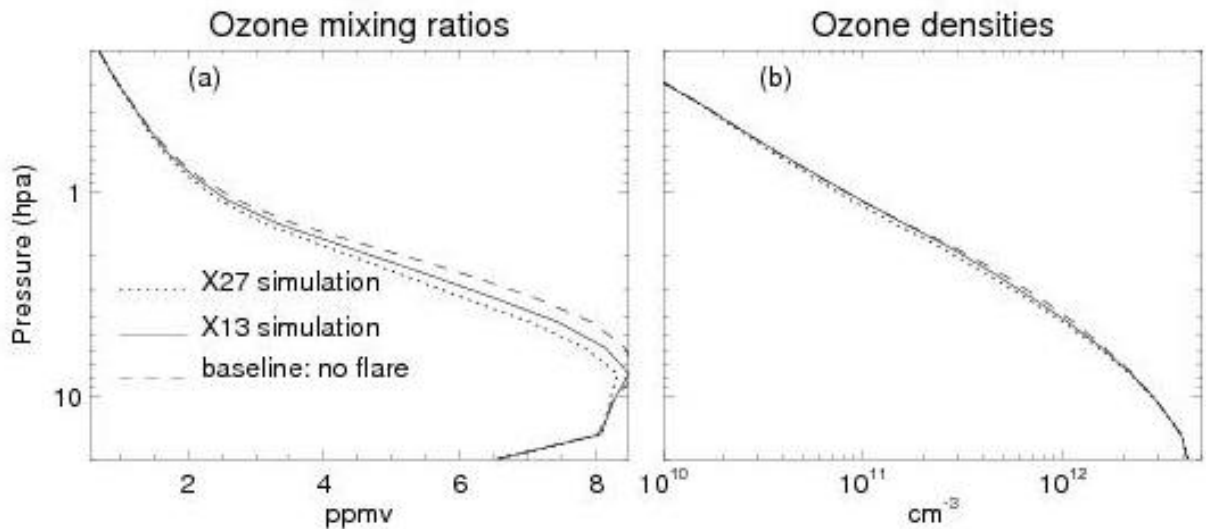
553 **Figure 11.** (a) Ratios of calculated ozone from CHEM1D compared with a baseline (no flare) case for
554 September 2, at a latitude of 39S. The two solid lines use NO_x input according to the scaling ratios
555 shown in panel (b) The X13 scaling is based upon the NO_x shown in Figures 3-5. The X27 scaling is a
556 hypothesized extrapolation based upon Figure 8 and discussed in the text. Also shown as the dashed line
557 in panel (a) is the ozone ratio from the TIME-GCM as per the surface contour plots shown in Figure 6.

558

559 Figure 11 shows that for the X13 case, we could expect ozone depletions of up to 8% in the
560 upper stratosphere. For the more significant X27 case (i.e., for a more intense supernova X-ray
561 event), we might see ozone reductions of up to 15-18% in the upper stratosphere. Figure 11 also
562 shows the vertical profile of the TIME-GCM ozone reduction. It does not exactly match the
563 profiles from CHEM1D in terms of shape and altitude of peak reduction, but it is very close to
564 the X13 CHEM1D simulation in terms of giving a peak loss of 6-7% in the upper stratosphere.
565 The TIME-GCM result is useful because it allows our detailed CHEM1D calculations to be
566 placed in the global context shown in Figure 7.

567 Based upon Figure 11 and Figure 7, we can conclude that a supernova soft X-ray event could
568 cause widespread ozone loss in the 10-20% range in the upper stratosphere for late winter/early
569 spring in the Southern Hemisphere. While this would likely be easily observable with suitable
570 instrumentation, it is less likely to have a dramatic biospheric effect. This is because most of the
571 stratospheric ozone is found at altitudes from 20-35 km (5 hPa-50 hPa pressure levels). The
572 losses shown in Figure 11 are only the upper edge of that layer. This is shown in Figure 12,
573 which shows the actual ozone mixing ratios (panel (a)) and ozone density profiles (panel (b))
574 which correspond to the scaling ratios shown in Figure 10. In the case where the model output is
575 shown as ozone densities, the curves are almost indistinguishable. The change in the total
576 column ozone, which is most relevant for surface UV exposure, is 1% for the X13 simulation
577 and 2% for the X27 extrapolation.

578



579

580 **Figure 12.** Absolute ozone abundances corresponding to the ratios presented in Figure 10. The three
581 simulations are labeled in panel (a). They are identically shown in density units in Panel (b) but are
582 almost indistinguishable because the 8-15% reductions are very hard to see on a graph that covers over
583 two orders of magnitude.

584

585 5. Discussion and conclusions

586 Our results clearly suggest the strong possibility of globally widespread ozone loss in the upper
587 stratosphere, at least for a period of a couple of months in the Southern Hemisphere. However, at
588 the same time, we conclude that this is unlikely to have a global biospheric impact because the
589 depletion is limited to the upper edges of the ozone layer. This limitation is derived from our
590 simulations showing that, like the EPP-IE, the Xray-IE does not penetrate below 35-40 km on a
591 global basis. At polar latitudes, our results allow us to speculate that a supernova could greatly
592 exacerbate the ozone hole. Or even, for atmospheres without anthropogenic chlorine, create an
593 ozone hole. Indeed, it has already been noted that the EPP-IE has been confused with an

594 expansion of the ozone hole due to volcanic aerosols (cf. Siskind et al., 2000 and discussion
595 therein). However, since the hole is generally confined to the polar vortex, the effects of the
596 Antarctic ozone hole have not caused widespread global ecological destruction although regional
597 effects may be occurring (Robinson et al., 2024). There are likely other more subtle hypothesized
598 effects of the enhanced NO_x that we do not address. For example, we do see moderate NO_x
599 enhancements throughout the Northern Hemisphere and it has been suggested that EPP-IE in the
600 Northern Hemisphere has effects on stratospheric and possibly tropospheric meteorology
601 (Seppala et al., 2009). Our work here cannot rule this out for the Xray-IE.

602 Certainly, our results come with large uncertainties that would be useful to address. Perhaps the
603 biggest is that the TIME-GCM, with a bottom boundary above the peak of the ozone layer, is not
604 designed to study stratospheric chemistry. Moreover, the 30 km bottom boundary prevents us
605 from studying descent of NO_x enriched air down to the lower altitudes where the EPP-IE has
606 been observed in the SH polar vortex (Randall et al., 2007). Thus our comments about the ozone
607 hole are necessarily speculative. In addition, our simulation of the NO produced during solar
608 flares appears to be less than observed by SNOE. This might mean that the NO response to a
609 flare would be greater than we suggest, perhaps by as much as a factor of 2. Here it would be
610 very helpful if there were another dataset that could corroborate the NO response reported by
611 Rodgers et al., (2010). As we noted above, the local time of the sun-synchronous SNOE orbit
612 was ideal for observing solar flares. By contrast, more recent NO observations which are
613 summarized in Table 1 and Figure 3 of Emmert et al., (2022) are less well suited. Emmert et al.
614 (2022) show that, for example, the Atmospheric Chemistry Experiment (ACE) and the Solar
615 Occultation for Ice Experiment (SOFIE) on the NASA/AIM satellite used the technique of solar
616 occultation which by definition means sunrise or sunset. This type of observation is not well
617 suited to observing the effect from a flare that would be less noticeable at local sunset or sunrise.
618 Likewise, the ODIN satellite, which measured NO with the Sub-millimeter radiometer (SMR)
619 was in a dawn-dusk synchronous orbit. Based upon Emmert et al., (2022) it appears that only
620 MIPAS on the ENVISAT satellite was in a proper daytime orbit to see flares. An examination of
621 the MIPAS data might be an interesting test of some of our SNOE-based results.

622 Ultimately, however, even if we did underestimate the NO production by a factor of 2 or even 3,
623 the effects on the ozone column are likely not catastrophic because they will be limited to above
624 35-40 km. We point to the simulations of Thomas et al., (2007) of a possible solar proton event
625 that may have accompanied the 1859 Carrington flare event. Solar protons penetrate much
626 deeper into the stratosphere than soft X-rays and thus the effect on NO_x is more direct rather
627 than indirect as simulated here. Indeed, they obtained much larger NO_x increases down to 30 km
628 and localized ozone losses near 35-40 km of greater than 30%. Despite this greater increase in
629 NO_x and greater ozone loss, their calculated perturbation to the ozone column was less than 15%
630 because the bulk of the ozone density between 20-30 km remained unaffected from the proton
631 flux. More recently, Reddman et al., (2023) performed a similar simulation of an extreme solar
632 proton event combined with an extreme geomagnetic storm. They show dramatically enhanced
633 ionization in the high latitude regions for all altitudes above 30 km. Their extrapolated NO_x
634 production is approximately 25-30 GM roughly equivalent to our extrapolation for our X27 case,
635 but now occurring directly at higher latitudes where transport to the lower stratosphere might be

636 hypothesized as more efficient. However, like our results, they find the overall impact of any
637 resulting ozone reduction on UV flux to the surface to be limited to less than 5%. The Reddman
638 simulation is important because it might be relevant to the question of whether a supernova
639 occurring out of the ecliptic plane and focused more on the higher latitudes where transport is
640 more efficient, could have a greater impact. Extrapolating from Reddman et al., (2023) we
641 argue that having greater ionization at higher latitudes above 30 km is still inefficient for
642 destroying global ozone which is concentrated at lower latitudes and at altitudes below 30 km.

643 By contrast, other phenomena linked to supernovae, such as gamma rays and cosmic rays, are
644 known to be absorbed by the atmosphere near the peak of the ozone layer in the 20-30 km
645 altitude range (Melott et al., 2017) and at lower latitudes. Therefore, in our assessment, those are
646 likelier candidates for causing global ozone destruction that would greatly enhance the flux of
647 destructive UV radiation to the surface. However, we should conclude by noting that even in
648 those cases, the destructiveness of both the gamma ray and cosmic ray mechanisms have also
649 been recently called into question (Christoudias et al., 2024). Our calculations here are therefore
650 consistent with Christoudias et al., (2024) in showing how the earth's atmosphere can shield its
651 biosphere.

652

653 *Code and Data Availability.* The TIME-GCM code is available by contacting the National Center for
654 Atmospheric Research. The model output produced herein is reproducible from the TIME-GCM model
655 source code following the discussions and implementations of the nudging schemes and lower boundary
656 conditions described thoroughly in Sections 2.4 and in Jones Jr. et al. (2018) and Jones Jr. et al. (2020).
657 Daily NCAR TGCMs outputs in netCDF format from this study are archived on the DoD HPCMP long-
658 term storage system. MERRA-2 middle atmospheric horizontal winds and temperatures used for
659 constraining TIME-GCM dynamics are available at [https://disc.gsfc.nasa.gov/datasets?project=MERRA-](https://disc.gsfc.nasa.gov/datasets?project=MERRA-2)
660 [2](https://disc.gsfc.nasa.gov/datasets?project=MERRA-2). The SABER and MLS data used in Figure 9 were respectively obtained from [https://saber.gats-](https://saber.gats-inc.com/)
661 [inc.com/](https://saber.gats-inc.com/) and <https://mls.jpl.nasa.gov/eos-aura-mls/data.php>. Other model output such as CHEM1D and
662 specific supernova output from TIMEGCM are both available in separately labeled folders on
663 <https://map.nrl.navy.mil/map/pub/nrl/>. The /chem1d folder contains the source code of the model and
664 there are text files for running the supernova simulations. The /timegcm_supernova folder contains
665 python compatible IDL save files of both TIMEGCM output and the NRLFLARE simulations along with
666 text files describing them.

667 *Author Contributions.* DES conceived the study, performed the analysis of the TIMEGCM
668 output, conducted the CHEM1D analysis and led the writing. MJJr. configured the TIMEGCM, both to be
669 nudged by MERRA and to input the NRLFLARE spectra, performed the simulations and wrote Section
670 2.2. JWR is the developer of NRLFLARE; he provided the soft X-ray spectra used by the TIMEGCM and
671 wrote Section 2.1.

672

673 *Competing Interests* The contact author has declared that none of the authors has any competing interests.

674

675 *Acknowledgements.* This work was supported by the Office of Naval Research. We also acknowledge the
676 NASA Living with a Star program for supporting development of NRLFLARE and the development of
677 the supernovae soft X-ray spectra. Computational resources for this work were provided by the U.S.
678 Department of Defense (DoD) High Performance Computing Modernization Program (HPCMP).

679

680 *Financial support.* This research has been supported by the Office of Naval Research (6.1
681 funding).
682

683 **References**

- 684
685 Airapetian, V. S., Barnes, R., Cohen, O., Collinson, G. A., Danchi, W. C., Dong, C. F., Del
686 Genio, A. S. D., France, K., Garcia-Sage, K., Glocer, A., Gopalswamy, N., Grenfell, J. L.,
687 Gronoff, G., Gudel, M., Herbst, K., Henning, W. G., Jackman, C. H., Jin, M., Johnstone, C. P.,
688 Kaltenecker, L., Kay, C. D., Kobayashi, K., Kuang, W., Li, G., Lynch, B. J., Luftinger, T.,
689 Luhmann, J. G., Maehara, H., Mlynczak, M. G., Notsu, Y., Osten, R. A., Ramirez, R. M.,
690 Rugheimer, S., Scheucher, M., Schlieder, J. E., Shibata, K., Sousa-Silva, C., Stamenkovic, V.,
691 Strangeway, R. J., Usmanov, A. V., Vergados, P., Verkhoglyadova, O. P., Vidotto, A. A.,
692 Voytek, M., Way, M. J., Zank, G. P., and Yamashiki, Y., Impact of space weather on climate
693 and habitability of terrestrial-type exoplanets (2020), *Int'l Journal of Astrobiology*,
694 <https://doi.org/10.1017/S1473550419000132>, 2019.
695
696 Arnone E. and Hauchecorne A., Stratospheric NO_y species measured by MIPAS and GOMOS
697 Onboard ENVISAT 2002-2010: Influence of plasma processes onto the observed distribution
698 and variability, *Space Sci Rev.*, 168, 315-332, DOI 10.1007/s11214-011-9861-1, 2011.
699
700 Bertaux, J. L., Hauchecorne, A., Lefevre, F., Breon, F. M., Blanot, L., Jouget, D., Lafrique, P.
701 and Akaev, P., The use of the 1.27 μm O₂ absorption band for greenhouse gas monitoring from
702 space and application to MicroCarb. *Atmospheric Measurement Techniques*, 13(6), 3329–3374.
703 <https://doi.org/10.5194/amt-13-3329-2020>, 2020.
704
705 Bradshaw, S. J. and Cargill, P. J., “The Influence of Numerical Resolution on Coronal Density in
706 Hydrodynamic Models of Impulsive Heating”, *The Astrophysical Journal*, vol. 770, no. 1, IOP,
707 doi:10.1088/0004-637X/770/1/12., 2013.
708
709 Brasseur G. and S. Solomon, 2005, *Aeronomy of the Middle Atmosphere*, D. Reidel Publishing
710 Co.
711
712 Brunton, I. R., O’Mahoney, C., Fields, B. D., Melott, A. L., and Thomas, B. C., X-Ray-luminous
713 Supernovae: Threats to terrestrial biospheres, *Astrophys. J.*, 947:42,
714 <https://doi.org/10.3847/1538-4357/acc728>, 2023.
715
716 Cliver, E. W., Schrijver, C. J., Shibata, K., and Usoskin, I. G., “Extreme solar events”, *Living*
717 *Reviews in Solar Physics*, vol. 19, no. 1, doi:10.1007/s41116-022-00033-8, 2022.
718
719 Christoudias, T., Kirkby, J., Stolzenburg, D., Pozzer, A., Sommer, E., Brassuer, G. P., Kulmala,
720 M., Lelieveld, J., Earth’s atmosphere protects the biosphere from nearby supernovae, *Nature*
721 *Communications: Earth and Environment*, <https://doi.org/10.1038/s43247-024-01490-9>, 2024.
722
723 Diouf M. M. N., Lefevre, F., Hauchecorne, A., and Bertaux, J.L., Three-Dimensional Modeling
724 of the O₂(¹Δ) Dayglow: Dependence on Ozone and Temperatures, *J. Geophys. Res.*,
725 <https://doi.org/10.1029/2023JD040159>, 2024.

726
727 Eckermann, S. D., Ma, J., Hoppel, K.W., Kuhl, D. D., Allen, D. R., Doyle, J. A., Viner, K. A.,
728 Ruston, B. C., Baker, N. L., Swadley, S. D., Whitcomb, T. R., Reynolds, C. A., Xu, L., Kaifler,
729 N., Reid, I. M., Murphy, D. J., and Love, P. T., High-altitude (0–100 km) global atmospheric
730 reanalysis system: Description and application to the 2014 austral winter of the deep propagating
731 gravity wave experiment (DEEPWAVE), *Monthly Weather Review*, 146(8), 2639–2666.
732 <https://doi.org/10.1175/MWR-D-17-0386.1>, 2018.
733
734 Ejzak, L. M., Melott, A. L., Medved, M. V., and Thomas B. C., Terrestrial consequences of
735 spectral and temporal variability in ionizing photon events, *ApJ*, 64,373,. 2007,
736 doi:10.1086/509106
737
738 Emmert, J. T., Jones, M. Jr., Siskind D. E., Drob D. P., Picone, J. M., Stevens M. H., Bailey S.
739 M., Bender, S., Bernath, P. F., Funke, B., Hervig, M. E., and Perot, K., NRLMSIS 2.1: An
740 empirical model of NO incorporated into MSIS, *J. Geophys. Res.*, 127, e2022JA030896.
741 <https://doi.org/10.1029/2022JA030896>, 2022.
742
743 Fletcher, L., Dennis, B. R., Hudson, H. S., Krucker, S., Phillips, K., Veronig, A., Battaglia, M.,
744 Bone, L., Caspi, A., Chen, Q., Gallagher, P., Grigis, P. T., Ji, H., Liu, W., Milligan, R. O., and
745 Temmer, M., “An Observational Overview of Solar Flares”, *Space Science Reviews*, vol. 159,
746 no. 1–4, pp. 19–106, doi:10.1007/s11214-010-9701-8, 2011.
747
748 Funke, B., Lopez-Puertas, M., Gil-Lopez, S., von Clarmann, T., Stiller, G. P., Fischer, H.,
749 Kellman, S., (2005) Downward transport of upper atmospheric NO_x into the polar stratosphere
750 and lower mesosphere during the Antarctic 2003 and Arctic 2002/2003 winters, *J. Geophys Res.*,
751 D240308, 0148-0227/05/2005JD006463
752
753 Funke, B., Lopez-Puertas M., Stiller, G. P. and von Clarmann, T., (2014) Mesospheric and
754 stratospheric NO_y produced by energetic particle precipitation during 2002–2012, *J. Geophys.*
755 *Res*, 119, 4429, 10.1002/2013JD021404
756
757 Funke B., Ball, W., Bender, S., Gardini, A., Harvey, V. L., Lambert, A., Lopez-Puertas, M.,
758 Marsh, D. R., Meraner, K., Nieder, H., Palvarinta, S-M., Perot, K., Randall, C. E., Reddman, T.,
759 Rozanov, E., Schmidt, H., Seppala, A., Sinnhuber, M., Sukhodolov, T., Stiller, G. P., Tsvetkova,
760 N. D., Verronen, P. T., Versick, S., von Clarmann, T., Walker, K. A., and Yushkov, V., (2017)
761 HEPPA-II model–measurement intercomparison project: EPP indirect effects during the
762 dynamically perturbed NH winter 2008–2009, *Atmos. Chem. Phys*, 17, 3573-3604,
763 doi:10.5194/acp-17-3573-2017.
764
765 Garcia, H. A., “Temperature and Emission Measure from Goes Soft X-Ray Measurements”,
766 *Solar Physics*, vol. 154, no. 2, pp. 275–308, 1994. doi:10.1007/BF00681100.
767
768 Garcia-Sage, K, Farrish A.O, Airapetian, V. S., (2023), Star-exoplanet interactions, A growing
769 interdisciplinary field in heliophysics, *Frontiers in Astronomy and Space Science*, vol. 10, doi:
770 10.3389/fspas.2023.1064076
771

772 Gehrels, N., Laird, C. M. Jackman, C. H., Cannizzo, J. K., Mattson, B., J., and Chen, W., Ozone
773 depletion from nearby supernovae, *The Astrophysical Journal.*, 585:1169-1176, 2003.
774

775 Gelaro, R., McCarty, W., Suarez, M. J., Todling, R., Molod, A., Takacs, L., Randles, C. A.,
776 Darmenov, A., Bosilovich, M. G., Reichle, R., Wargan, K., Coy, L., Cullather, R., Draper, C.,
777 Akella, S., Buchard, V., Conaty, A., DaSilva, A.M., Gu, W., Kim, G-K., Koster, R., Lucchesi,
778 R., Merkova, D., Nielsen, J. E., Partyka, G., Pawson, S., Putman, W., Rienecker, M., Schubert,
779 S. D., Sienkiewicz, M., and Zhao, B., The modern-era retrospective analysis for research and
780 applications, version 2 (MERRA-2), *J. Clim.*, 30(14), 5419–5454, doi:10.1175/JCLI-D-16-
781 0758.1, 2017.
782

783 Jones, M., D. P. Drob, D. E. Siskind, J. P. McCormack, A. Maute, S. E. McDonald, and K. F.
784 Dymond, Evaluating Different Techniques for Constraining Lower Atmospheric
785 Variability in an Upper Atmosphere General Circulation Model: A Case Study During the
786 2010 Sudden Stratospheric Warming, *J. Adv. Model. Earth Syst.*, 10(12), 3076–3102,
787 doi:10.1029/2018MS001440, 2018
788

789 Jones, M. Jr., Goncharenko, L. P., McDonald, S. E., Zawdie, K. A., Tate, J., Gasperini, F.,
790 Pedatella, N. M., Drob, D. P., and McCormack, J. P., Understanding nighttime ionospheric
791 depletions associated with sudden stratospheric warmings in the American sector. *Journal of*
792 *Geophysical Research: Space Physics*, 128, e2022JA031236.
793 <https://doi.org/10.1029/2022JA031236>, 2023
794

795 Jones, M. Jr., Siskind, D. E., Drob, D. P., McCormack, J. P., Emmert, J. T., Dhadly, M. S.,
796 Attard, H. E., Mlynczak, M. G., Brown, P. G., Stober, G., Kozlovsky, A., Lester, M., Jacobi, C.,
797 Coupling from the middle atmosphere to the exobase: Dynamical disturbance effects on light
798 chemical species. *Journal of Geophysical Research: Space Physics*, 125, e2020JA028331.
799 <https://doi.org/10.1029/2020JA028331>, 2020
800

801 Kahler, S. W and Ling, A. G, Solar Stellar Connection: X-ray flares to energetic (> 10 MeV)
802 particle events, *Astrophys. J.*, 956, <https://doi.org/10.3847/1538-4357/acf1ff>, 2023
803

804 McCormack, J., Hoppel, K., Kuhl, D., deWit, R., Stober, G., Espy, P., Baker, N., Brown, P.,
805 Fritts, D., Jacobi, C., Janches, D., Mitchell, N., Ruston, B., Swadley, S., Viner, K., Whitcomb,
806 T., Hibbins, R., Comparison of mesospheric winds from a high-altitude meteorological analysis
807 system and meteor radar observations during the boreal winters of 2009–2010 and 2012–2013.
808 *Journal of Atmospheric and Solar-Terrestrial Physics*, 154, 132–166.
809 <https://doi.org/10.1016/j.jastp.2016.12.007>, 2017
810

811 Melott, A. L., Thomas, B. C., Kahcelriess, M., Semikoz, D. V., and Overholt A. C., A supernova
812 at 50 pc: Effects on the Earth’s atmosphere and biota, *Astrophys. J.*, 840,
813 <https://doi.org/10.3847/1538-4357/aa6c57>, 2017
814

815 Nedoluha G. N., Gomez, R. N, Boyd, I., Neal H., Parrish A., Connor B., Mooney T., Siskind, D.
816 E., Sagawa, H., and Santee, M., Initial Results and Diurnal Variations Measured by a New

817 Microwave Stratospheric ClO Instrument at Mauna Kea, *Journal Geophysical Research.*, 125,
818 <https://doi.org/10.1029/2020JD033097>, 2020
819

820 Neupert, W. M., Gates, W., Swartz, M., & Young, R., Observation of the solar flare X-ray
821 emission line spectrum of iron from 1.3 to 20 Å. *The Astrophysical Journal*, 149, L79–L83.
822 <https://doi.org/10.1086/180061>, 1967.
823

824 Pettit, J. M., Randall, C. E., Peck, E. D., Harvey, V. L., A new MEPED-based precipitating
825 electron data set, *J. Geophys. Res.*, <https://doi.org/10.1029/2021JA029666>, 2021.
826

827 Price, J. M., Mack, J. A., Rogaski, C. A. and Wodtke, A. M., Vibrational-state-specific self-
828 relaxation rate constant. Measurements of highly vibrationally excited O₂ (v=19-28), *Chemical*
829 *Physics.*, 175(1), 83-98, [https://doi.org/10.1016/0301-0104\(93\)80230-7](https://doi.org/10.1016/0301-0104(93)80230-7), 1993.
830

831 Qian L., Wang, W., Burns, A. G., Chamberlin, P. Coster, A., Zhang S-R., Solomon, S., Solar
832 Flare and Geomagnetic Storm Effects on the Thermosphere and Ionosphere During 6–11
833 September 2017, *J. Geophys. Res.*, 124, 1298, <https://doi.org/10.1029/2018JA026175>, 2019
834

835 Randall, C. E., Harvey, V. L., Singleton, C. S. Bernath, P., Boone, C. D., Kozyra, J. U.,
836 Enhanced NO_x in 2006 linked to strong upper stratospheric Arctic vortex, *Geophys. Res. Lett.*,
837 33, L18811, doi:10.1029/2006GL027160., 2006
838

839 Randall, C. E., Harvey, V. L., Singleton, C. S., Bailey, S. M., Bernath, P. F., Codrescu, M.,
840 Nakajima, H., Russell, J. M. III, Energetic particle precipitation effects on the Southern
841 Hemisphere stratosphere in 1992-2005 *J. Geophys. Res.*, 112., D08308,
842 doi:10.1029/2006JD007696, 2007.
843

844 Reddmann, T., Sinnhuber, M., Wissing, J.M., Yakovchuk, O., and Usoskin, I., The impact of an
845 extreme solar event on the middle atmosphere: a case study, *Atmos. Chem. Phys.*, 23, 6989-
846 7000., 2023, <https://doi.org/10.5194/acp-23-6989-2023>.

847 Redmon, R. J., Seaton, D. B., Steenburgh, J. R., He, J., & Rodriguez, J. V., September 2017's
848 geoeffective space weather and impacts on Caribbean radio communications during hurricane
849 response. *Space Weather*, 16(9), 1190–1201, <https://doi.org/10.1029/2018SW001897>, 2018.

850 Reep, J. W., and Airapetian, V., Understanding the duration of solar and stellar flares at various
851 wavelengths, *Astrophys. J.*, vol. 98, DOI 10.3847/1538-4357/acf45a, 2023.

852 Reep, J. W., Bradshaw, S. J., Crump, N. A., and Warren, H. P., “Efficient Calculation of Non-
853 local Thermodynamic Equilibrium Effects in Multithreaded Hydrodynamic Simulations of Solar
854 Flares”, *The Astrophysical Journal*, vol. 871, no. 1, IOP, doi:10.3847/1538-4357/aaf580., 2019.

855 Reep, J. W., Siskind, D. E., and Warren, H. P., “Solar Flare Irradiance: Observations and
856 Physical Modeling”, *The Astrophysical Journal*, vol. 927, no. 1, IOP, doi:10.3847/1538-
857 4357/ac4784, 2022.

858 Reep, J. W., Warren, H. P., Moore, C. S., Suarez, C., and Hayes, L. A., “Simulating Solar Flare
859 Irradiance with Multithreaded Models of Flare Arcades”, *The Astrophysical Journal*, vol. 895,
860 no. 1, IOP, doi:10.3847/1538-4357/ab89a0., 2020

861
862 Robinson, S. A, Revell, L. E., Mackenzie, R., Ossala, Extended ozone depletion and reduced
863 snow and ice cover- Consequences for Antarctic biota, *Global Change Biology*,
864 <https://doi.org/10.1111/gcb.17283>., 2024.

865
866 Roble, R. G., and Ridley, E. C., A thermosphere-ionosphere-mesosphere-electrodynamics-
867 General Circulation Model (TIME-GCM): Equinox solar cycle minimum simulations (30-500
868 km), *Geophys. Res. Lett.* 417-420, 1994

869
870 Rodgers, E. M., Bailey, S. M., Warren, H. P., Woods, T. N., and Eparvier, F. G., Nitric oxide
871 density enhancements due to solar flares, *Adv. Sp. Res.*, 45,28-38, 2010.

872
873 Seppala, A., Randall, C. E., Clilverd, M. A., Rozanov, E., and Rodger, C. J., Geomagnetic
874 activity and polar surface air temperature variability, *J. Geophys. Res.*, 114,
875 <https://doi.org/10.1029/2008JA014029>, 2009.

876
877 Siskind, D. E., Bacmeister, J. T., Summers M. E., and Russell J.M. III, Two-dimensional model
878 calculations of nitric oxide transport in the middle atmosphere and comparison with Halogen
879 Occultation Experiment data, *Journal of Geophysical Research*, 102/D3, 3527-3545.f, 1997.

880
881 Siskind, D. E., Nedoluha, G. N, Randall, C. E., Fromm, M. and Russell, J. M. III, An assessment
882 of Southern Hemisphere stratospheric NOx enhancements due to transport from the upper
883 atmosphere, *Geophys. Res. Lett.*, 329-332, 2000.

884
885 Siskind, D. E., Stevens, M. H., Englert, C. R. and Mlynczak M. G., Comparison of a
886 photochemical model with observations of mesospheric hydroxyl and ozone, *J. Geophys. Res.*,
887 118, 195–207, doi:10.1029/2012JD017971, 2013.

888
889 Siskind, D. E., Jones, M., Jr., Reep., J. W., Drob, D. P. Samaddar, S., Bailey, S. M., and Zhang,
890 S-R., Tests of a new solar flare model against D and E region ionospheric data., *Sp. Wea.*, 2,
891 e2021SW003012, <https://doi.org/10.1029/2021SW003012>, 2022.

892
893 Slinger, T. G., L.E. Jusinski, G. Black and G. E. Gadd, Vibrationally excited O₂, *Science*, 241,
894 945, 1988.

895
896 Solomon, S. C., and Qian L., Solar extreme-ultraviolet irradiance for general circulation models,
897 *Journal of Geophysical Research*, 110, A10306, <https://doi.org/10.1029/2005JA011160>, 2005.

898
899 Solomon S., Roble, R. G., and Crutzen, P. J., Photochemical Coupling Between the
900 Thermosphere and the Lower Atmosphere, 1. Odd nitrogen from 50 to 120 km, *J. Geophys. Res.*,
901 87, C9, 7206-7220, 1982.

902
903 Stauffer, D. R., and Seaman, N. L., Use of four-dimensional data assimilation in a limited-area
904 mesoscale model. Part I: Experiments with synoptic-scale data. *Monthly Weather Review*,

905 118(6), 1250–1277. [https://doi.org/10.1175/1520-0493\(1990\)118<1250:UOFDDA>2.0.CO;2](https://doi.org/10.1175/1520-0493(1990)118<1250:UOFDDA>2.0.CO;2),
906 1990.
907
908 Stauffer, D. R., and Seaman, N. L., Multiscale four-dimensional data assimilation. *Journal of*
909 *Applied Meteorology*, 33(3), 416–434,
910 [https://doi.org/10.1175/15200450\(1994\)033<0416:MFDDA>2.0.CO;2](https://doi.org/10.1175/15200450(1994)033<0416:MFDDA>2.0.CO;2), 1994.
911
912 Thomas B.C., Jackman, C. H., and Melott, A.L., Modeling atmospheric effects of the September
913 1859 solar flare, *Geophys. Res. Lett.*, 34, L06810, doi:10.1029/2006GL029174,2007.
914
915 Vink, J., “Supernova remnants: the X-ray perspective”, *Astronomy and Astrophysics Review*,
916 vol. 20, Springer, doi:10.1007/s00159-011-0049-1., 2012.
917
918 Vitt, F.M. and Jackman, C. H., A comparison of sources of odd nitrogen production from 1974
919 through 1993 in the Earth's middle atmosphere as calculated using a two-dimensional model, *J.*
920 *Geophys. Res.*, 101, 6729, doi:10.1029/95JD03386, 1996.
921
922 Zhang, X., Forbes, J. M., and Hagan, M. E., Longitudinal variation of tides in the MLT region: 1.
923 Tides driven by tropospheric net radiative heating. *Journal of Geophysical Research*, 115,
924 A06316. <https://doi.org/10.1029/2009JA014897>, 2010a
925
926 Zhang, X., Forbes, J. M., and Hagan, M. E., Longitudinal variation of tides in the MLT region: 2.
927 Relative effects of solar radiative and latent heating. *Journal of Geophysical Research*, 115,
928 A06317. <https://doi.org/10.1029/2009JA014898>, 2010b
929
930